Journal of Energy Storage 175 (2026) 123289

Contents lists available at ScienceDirect

Journal of Energy Storage

journal homepage: www.elsevier.com/locate/est

Research Papers

Enhancement of pressure-tank release characteristics for supercritical CO_2 compressed energy storage systems using built-in heat storage materials

Xin Yan [a,*], Lulu Xing [a], Yuqian Zhang [a], Jinliang Xu [a,b], Rui Wu [a], Helong Su [a]

[a] Beijing Key Laboratory of Multiphase Flow and Heat Transfer for Low Grade Energy Utilization, North China Electric Power University, Beijing, 102206, China
[b] Key Laboratory of Power Station Energy Transfer Conversion and System, North China Electric Power University, Ministry of Education, Beijing, 102206, China

ARTICLE INFO

Keywords:
Compressed CO_2 energy storage
Pressure storage tanks
Pseudo phase change
Built-in thermal storage
Energy storage density

ABSTRACT

The supercritical CO_2 (sCO_2) compressed energy storage (CCES) system offers high efficiency and equipment compactness, but its energy storage density (ESD) is constrained by strong coupling between temperature and pressure of sCO_2 in constant-volume pressure storage tanks (PST). Pressure variations induce temperature changes, which subsequently modify the density and further amplify the pressure fluctuation, causing the PST to reach its cut-off pressure earlier and constraining further improvement in ESD. While variable-volume tanks can achieve constant-pressure operation and improve sCO_2 utilization, their engineering complexity restricts large-scale deployment. To address this challenge, a regenerative pressure storage tank (R-PST) was proposed, which co-stores heat and pressure via embedding heat-storage material (HSM) in a constant-volume PST. The HSM stores the thermal energy converted by flow work during the charging process and returns it to the sCO_2 during discharge. The recovered heat effectively mitigates the temperature and pressure drop of the sCO_2 throughout the discharge phase, thereby enabling deeper expansion and increasing the total amount of working fluid released. Using copper foam as the HSM and operating between an initial pressure of 15 MPa and a cut-off pressure of 13 MPa, the R-PST releases an additional 16.9 tons of sCO_2, representing a 57.2% improvement over a conventional PST. The R-PST also achieves higher mass flow rates and longer discharge duration. A sensitivity analysis evaluates the influence of initial pressure, working pressure differential, and HSM parameters on discharge behavior. In addition, the CCES system coupled with the R-PST achieves a 15.3% improvement in ESD. Overall, this work offers a practical and scalable pathway for improving the ESD, and advancing the efficiency and engineering applicability of next-generation CCES technologies.

0. Introduction

Electricity is the most important secondary energy for global economic development, and most of it is still generated from fossil fuels [1]. Over the past two centuries, the rapid consumption of traditional fossil resources has caused global issues such as climate warming, environmental pollution, and energy crises [2]. So, the share of renewable energy in power generation has grown rapidly. However, wind and solar power are inherently intermittent, fluctuating, and cyclical, creating challenges for power balance, grid stability, and dispatch operations [3,4]. To overcome these problems, various energy storage technologies have been developed. Among them, compressed gas energy storage (CGES) has attracted significant attention due to its high energy density, long operation life, and environmental friendliness [5]. CGES converts electrical energy into gas pressure potential via compressors and releases it by expanding the high-pressure gas through turbines to regenerate electricity [5]. Compressed air energy storage (CAES), as the most mature CGES technology, has been demonstrated in commercial plants such as Huntorf (Germany) [6] and Alabama (USA) [7]. However, air has an extremely low critical temperature (−140.6 °C), which makes it difficult to liquefy under ambient conditions. The volumetric energy density of CAES remains low (1.8–72.0 MJ/m^3) [8], limiting scalability for large-scale and long-duration storage.

Compared with air, CO_2 has a much higher critical temperature (31 °C) and a moderate critical pressure (7.38 MPa), enabling high-density storage under mild conditions. Compressed CO_2 energy storage (CCES) shows advantages over CAES in both cycle efficiency and volumetric energy density [9,10]. Moreover, CCES systems are compact and respond rapidly, making them suitable for applications such as grid load leveling, emergency backup, and renewable energy utilization

* Corresponding author.
E-mail address: yanxin@ncepu.edu.cn (X. Yan).

https://doi.org/10.1016/j.est.2026.123289
Received 29 December 2025; Received in revised form 27 April 2026; Accepted 22 June 2026
Available online 26 June 2026
2352-152X/© 2026 Elsevier Ltd. All rights are reserved, including those for text and data mining, AI training, and similar technologies.

[11]. Unlike CAES, CCES systems operate in a closed-loop, as CO_2 cannot be directly sourced from the environment. Therefore, the CO_2 storage tanks are required to act as the high-pressure and low-pressure chambers, whose operational parameters significantly affect system efficiency and energy density [12]. When the CCES operates in the supercritical region of CO_2, the pressure and temperature of sCO_2 in the fixed-volume tanks are strongly coupled: pressure changes induce temperature variations, which in turn exacerbate pressure fluctuations. Study shows that within the designed operation range of 2 MPa, the proportion of usable sCO_2 in a constant-volume pressure storage tank (PST) is as low as 5–10% when the initial pressure ranges from 10 to 20 MPa, severely limiting the energy storage density (ESD) and discharge duration of CCES systems [13].

To improve the working-fluid utilization and ESD, researchers have proposed constant-pressure tanks with variable-volume. Bartosz Stanek et al. [14] developed a variable-volume CO_2 storage device based on Pascal's law, in which a piston-rod mechanism balances forces between high- and low-pressure chambers, achieving constant-pressure energy release. With CO_2 parameters of 0.25 MPa/30 °C (low-pressure chamber) and 32.427 MPa/30 °C (high-pressure chamber), the CCES system achieved a cycle efficiency of up to 76% [14]. However, piston sealing and mechanical reliability issues limit its feasibility for large-scale applications, making it suitable only for small, distributed storage systems. Other researchers use external pressure sources to maintain constant storage pressure. Xu et al. [15] proposed a CCES system that places gas bladders at specific ocean depths, where hydrostatic pressure serves as a constant pressure source. Their system operated between 24.79 MPa/99.57 °C (high-pressure) and 7.57 MPa/35 °C (low-pressure), with an ESD of 28.4 MJ/m^3 and nearly 100% working-fluid utilization. Liu et al. [16] introduced aquifer-based geological formations acting as constant-pressure chambers, where crustal pressure provides the pressure source and groundwater seals CO_2 to prevent leakage. However, both methods depend heavily on external geological and environmental conditions, restricting their applicability. And the effectiveness of aquifer-based storage requires further study. Additionally, liquid CO_2 energy storage (LCES) systems have been proposed, in which CO_2 is stored in saturated liquid form [17,18]. During discharge, liquid CO_2 vaporizes and expands, mitigating tank pressure fluctuations and elevating the utilization of CO_2 [19]. However, LCES systems require external cooling to liquefy CO_2, increasing system complexity and limiting overall efficiency to below 60% typically [20,21]. From the analysis of the above studies, it can be concluded that minimizing the effect of the inflow and outflow of CO_2 per unit mass on the pressure of the PST is a key factor in improving the efficiency of fluid utilization and the ESD of CCES. In CCES, the constant-volume storage tank is currently the most widely adopted configuration. To address its low ESD, this study proposes a novel sCO_2 storage tank incorporating a built-in heat storage medium (HSM), referred to as the regenerated pressure storage tank (R-PST).

In a typical thermodynamic process, when gas flows out of a constant-volume storage tank, a portion of its internal energy is converted into flow work, resulting in a decrease in gas temperature. Consequently, apart from the pressure drop caused by the reduced gas mass, the remaining gas in the tank undergoes an additional pressure decrease due to its lower temperature. Chen et al. proposed an adiabatic compressed air energy storage system [22], in which the heat generated during air compression is stored externally in a thermal storage tank and later recovered via a heat exchanger during discharge to enhance the air's capacity for work output. Various configurations, such as internal fins [23], packed beds [24], and embedded thermal masses [25], have been investigated to improve heat storage and transfer performance within the external heat exchangers. However, these approaches cannot suppress the pressure decrease in the gas storage tank that results from the reduction of the internal energy of the remaining air. The innovation of the R-PST lies in its integration of an internal HSM that facilitates heat exchange with the sCO_2 inside the tank. This configuration replenishes the internal energy lost by the sCO_2 during expansion, thereby moderating its temperature drop and reducing the rate of pressure decline. In essence, the R-PST enables a "regeneration" of the internal energy and temperature of the sCO_2. For the charge process, as the sCO_2 enters the PST, the flow work it carries is converted into thermal energy, resulting in an increase in temperature and a corresponding extra rise in pressure. The built-in HSM in the R-PST absorbs part of this thermal energy, thereby moderating the temperature rise and slowing down the rate of pressure increase. The HSM decouples the positive feedback between temperature and pressure in sCO_2 tanks to a certain extent, improving the ESD of the CCES.

The main contributions of this study are as follows: 1) A novel sCO_2 storage tank with a built-in thermal energy storage medium is proposed, offering a simple and reliable route to enhance ESD in CCES systems. 2) A thermodynamic model of the R-PST is established. Under typical operating conditions, the sCO_2 utilization increases by 57.2%, and the temperature–pressure variation rate decreases by 42% compared with a PST without HSM. 3) From the thermophysical analysis, the HSM reduces temperature variations and weakens their effect on CO_2 density, making the discharge curve of sCO_2 closer to the $|\partial\rho/\partial P|_{\max} \sim P$. 4) A sensitivity analysis examines the effects of initial pressure, working pressure differential, and the properties of HSM on discharge characteristics. The structure of this paper is organized as follows: Section 1 introduces the simplified computational model and the discharge characteristics of a conventional PST; Section 2 presents the computational model of the proposed R-PST and analyzes its discharge behavior; Section 3 conducts a parametric sensitivity analysis for the R-PST; Section 4 demonstrates the improvement in the energy charging and discharging performance of a practical CCES system when coupled with the R-PST; Finally, Section 5 discusses the current limitations of this work and outlines prospects for future research. The proposed sCO_2 tank with the built-in HSM achieves higher energy density without requiring complex volume-changing mechanisms. It can be seamlessly integrated into existing CCES architectures, offering a promising pathway toward efficient and scalable energy storage.

1. The characteristics of conventional PST

To investigate the characteristics of R-PST, it is necessary to analyze and clarify the energy charging and discharging characteristics of the conventional PST first. Since the charging and discharging processes of PST are inverse to each other, this study focuses primarily on the discharging process as a representative case. The results obtained herein are equally applicable to the charging process of PST.

1.1. The computational model and assumptions

The cycle of CCES typically consists of eight components: a high-pressure tank (H-PST), a low-pressure tank (L-PST), a turbine, a compressor, two heat exchangers (HE), a hot tank (HT), and a cold tank (CT) [12], as shown in Fig. 1a. The two heat exchangers and the two thermal storage tanks are applied to recovery compression heat and warm the CO_2 released from H-PST improving the cycle efficiency. The H-PST operates at constant volume with variable pressure, whereas the L-PST is a flexible airbag in which the pressure remains constant at atmospheric pressure.

In this study, the typical *P-T* diagram of the CCES cycle is shown in Fig. 1b, which is a transcritical cycle. It should be noted that the compression and expansion processes are not the focus of this study. Thus, the compression and expansion processes in Fig. 1b are simplified to one stage. In practice, these processes occur in multiple stages due to the large pressure difference involved [12,18]. The H-PST is operated in a range of 8–20 MPa, which is in a supercritical state. There is no throttle valve at the outlet of H-PST to regulate flow. The pressure of L-PST is constant at atmospheric pressure. The outlet flow rate of H-PST is entirely determined by the turbine's structural and operating parameters. Here, the H-PST is decoupled from the CCES system to be

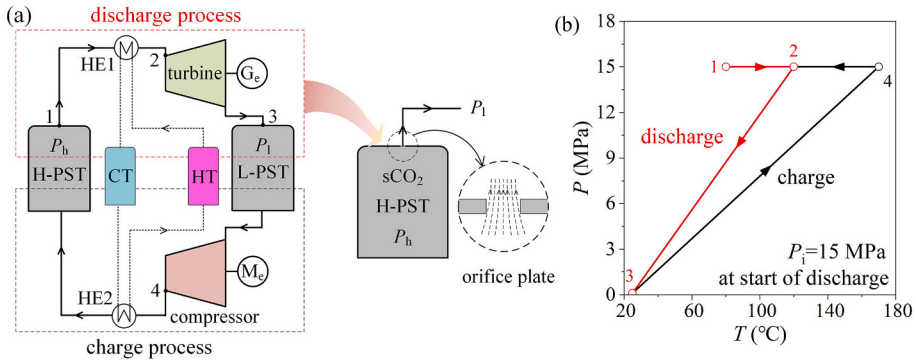


Fig. 1. The typical cycle of CCES (a, the model of the compressed carbon dioxide energy storage system and the simplified presentation of the high-pressure tank. H-PST: high-pressure tank, L-PST: low-pressure tank, HE: heat exchanger, HT: hot tank, CT cold tank. P_h and P_l are the pressures in H-PST and L-PST, respectively. The G_e is the Generator, and the M_e is the electric motor. b, the *P-T* diagram of the CCES cycle with $P_i = 15$ MPa at start of discharge or finish of charge. With the charge and discharge process, the pressure of H-PST will change. The P_i is the initial pressure of the H-PST).

independently analyzed. Under a fixed turbine rotational speed, the mass flow rate of the sCO_2 through the turbine decreases as the inlet–outlet pressure difference decreases [26]. The expansion and power output of sCO_2 outside the H-PST fall outside the scope of this study. The focus is on the thermophysical property changes of the sCO_2 inside the tank and the actual amount of working fluid released within the given operating pressure range. Thus, to further simplify the model, the pressure difference-flow coupling of the turbines is represented using an orifice-plate pressure-difference-flow model, as shown in Fig. 1a. It should be noted that this substitution is intended only to qualitatively simulate the trend of decreasing outlet mass flow rate with decreasing pressure difference. The resulting outlet mass flow rate does not reflect the actual turbine performance.

The lumped parameter method is used to model the dynamical release characteristics of PST [26]. The assumptions and boundary conditions of the transient discharge model of the H-PST are as follows:

1. The PSTs are usually externally insulated to prevent heat loss from the working fluid [26]. Thus, the discharge process is adiabatic. The temperature variations of the sCO_2 are caused solely by expansion or compression.
2. The sCO_2 inside the storage tank is isothermal and homogeneous.
3. The outlet pressure of the storage tank during the release process is constant at 101.325 kPa.
4. The outlet mass flow rate of sCO_2 is calculated using the orifice flow model.
5. The discharge process ends when the pressure in the tank drops to a cut-off pressure P_e.

Based on the laws of mass and energy conservation, the transient thermodynamic model of sCO_2 discharge from a conventional PST is expressed as follows [26]:

$$Gu_c + m_c\frac{du_c}{dt} = Gh_c \tag{1}$$

$$m_c = m_{c,i} - \int_0^t G dt \tag{2}$$

where u_c denotes the specific intrinsic energy of sCO_2, m_c is the mass of sCO_2 in the PST, h_c is the specific enthalpy, $m_{c,i}$ is the mass of sCO_2 in the PST at initial time, t is the releasing time, and G is the mass flow rate, determined using the orifice flow model [27]:

$$G = 0.61A_o\sqrt{2\rho_c(P_h - P_l)} \tag{3}$$

where A_o represents the PST outlet cross-sectional area ($A_o = 314\,cm^2$), corresponding to an outlet pipe of DN 20. The ρ_c is the sCO_2 density inside the tank, and P_h and P_l are the internal and external pressures of the tank, respectively.

Fig. 2 illustrates the computational procedure for the thermodynamic model of the conventional PST discharge process, which is a time-marching scheme. The thermophysical properties of sCO_2 are obtained from the NIST database [28], which provides higher accuracy compared with using an equation of state. Based on the initial conditions and flow rate G, the computation process is advanced step by step. At each time interval, the mass and specific intrinsic energy of the working fluid inside the tank are calculated. Then these values are used to call the NIST database to compute other thermodynamic properties, until the tank pressure drops to the cut-off pressure. Model validation is performed by comparing the results with a reference case from the literature [29], as shown in Fig. 3. It is noted that the CCES model in literature [29] employs a sliding-pressure and constant-mass-flow for discharge, whereas the model in this work adopts a sliding-pressure and variable-mass-flow discharge approach. Thus, during validation, the mass flow rate G in the model above is set equal to the value used in the reference [29]. The results from the proposed model and the reference match well. The maximum deviation occurs at $t = 13{,}677$ s, where the pressure error is 0.116 MPa (relative error 3.49%), corresponding to the temperature

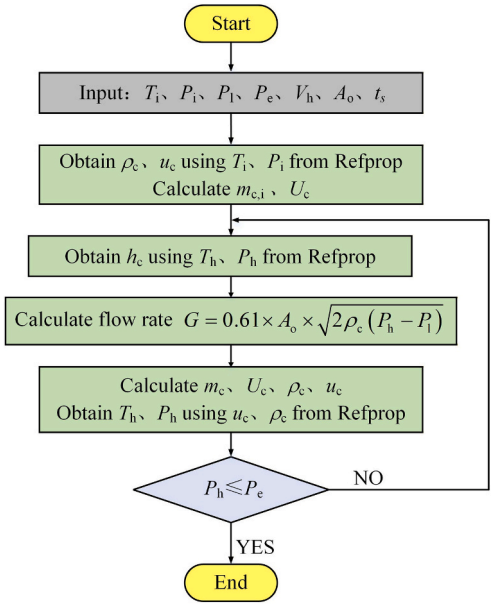


Fig. 2. Computational flowchart of the release process in a traditional high-pressure tank.

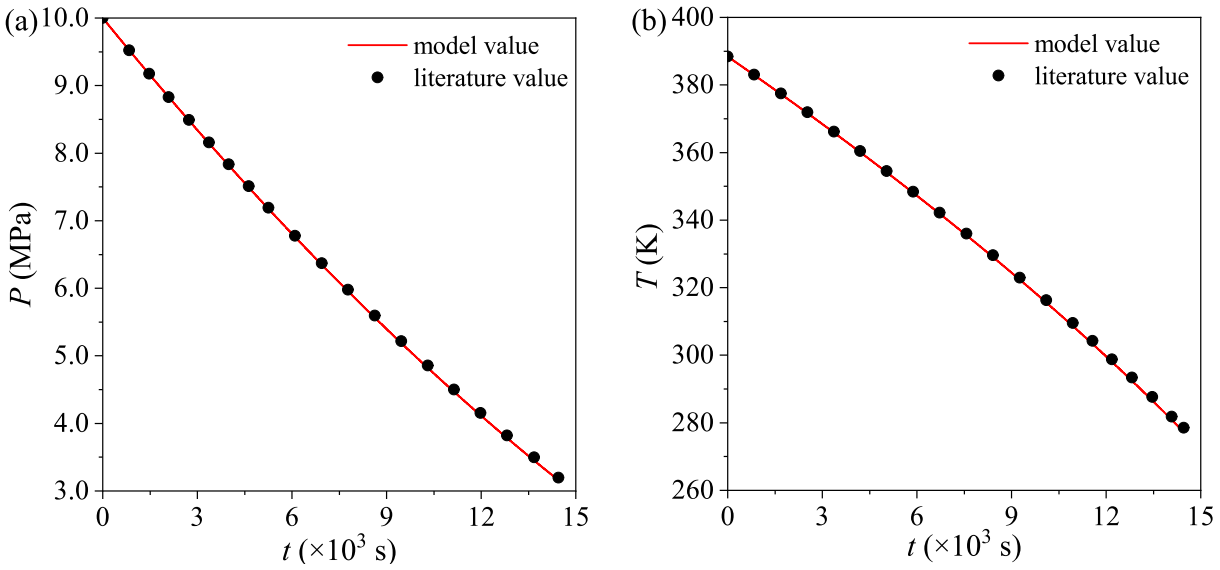


Fig. 3. The verification of model calculation results. (a and b are verified for the pressure and temperature of the work fluid in the tank, respectively.)

error of 1.07 K (relative error 0.38%). These results confirm the accuracy and reliability of the proposed model of tank and its computational results.

The energy storage density (ESD) is defined as the amount of energy stored per unit volume, considering only the turbine work output and the total tank volume [12]. The ESD is calculated as

$$\omega = \frac{W_T}{V} = \frac{\int_0^t G(h_{t0} - h_{t1})\,dt}{V_{L\text{-}PST} + V_{H\text{-}PST}} \tag{4}$$

where the W_T is the work output of turbine, V is the total tank volume containing L-PST and H-PST. The h_{t0} and h_{t1} are the CO_2 specific enthalpies at the inlet and outlet of the turbine, respectively. $V_{L\text{-}PST}$ and $V_{H\text{-}}$

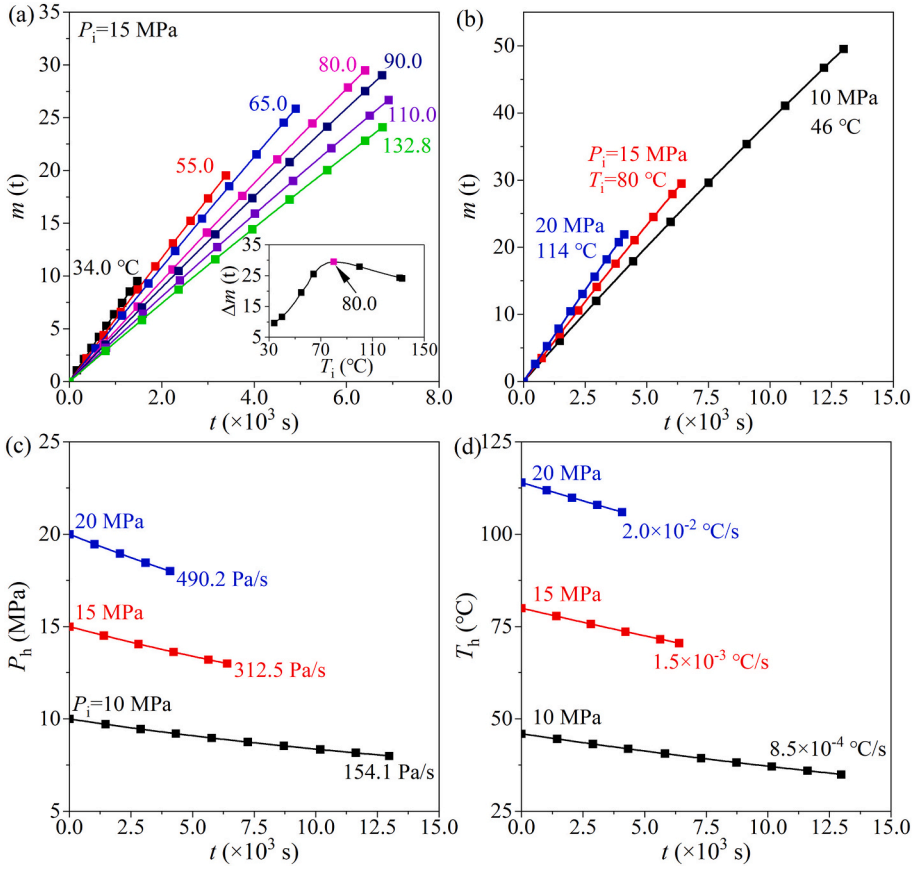


Fig. 4. Release characteristics of working fluid in a traditional high-pressure tank. (a is the released mass curves of working fluid for different initial temperatures; the insert figure is the released mass of working fluid versus initial temperature. b is the optimal released-mass curves at initial pressures of 10, 15, and 20 MPa. c is the pressure versus time at 10, 15, and 20 MPa. d is the temperature versus time at 10, 15, and 20 MPa.)

PST are the volumes of the low-pressure storage tank and high-pressure storage tank, respectively.

1.2. The discharge characteristics

In this study, the pressure storage tank is designed with a volume of 1000 m^3. It is a spherical tank with a diameter of ~14.4 m. The working pressure difference ($\Delta P = P_i - P_e$) during discharge is set to 2 MPa. Since the ESD is positively correlated with the released mass of the CO_2 for a certain initial pressure P_i, the released mass is chosen as the primary evaluation parameter. Fig. 4 shows the effects of different initial temperatures and pressures on the discharge characteristics. The influence of the initial temperature on the mass release process is illustrated in Fig. 4a. The slope of each curve represents the mass flow rate G. As the initial temperature T_i increases, the density of the sCO_2 inside the tank decreases, leading to a reduction in mass flow rate. And the total released mass Δm first increases and then decreases, reaching a maximum at T_i = 80 °C. Fig. 4b shows the discharge processes at different initial pressures (P_i = 10 MPa, 15 MPa, and 20 MPa), each curve corresponding to its optimal case, which has the largest released mass. For every initial pressure, there exists an optimal temperature that maximizes the released mass. The optimal temperature results from the competition between two opposing effects: As temperature rises, the internal energy of the sCO_2 increases, allowing it to maintain better expansion characteristics, thereby slowing the rate of pressure drop, extending the duration time of PST working, and increasing the total released mass. However, higher temperatures reduce the density of the sCO_2 inside the tank, decreasing the stored mass for a given PST volume, which in turn reduces the total releasable mass. These two competing effects determine that there exists an optimal temperature that maximizes the total released mass of the sCO_2 for a given initial pressure. The optimal temperature rises with increasing initial pressure, while the total released mass decreases.

The temporal variations of pressure and temperature inside the tank are shown in Fig. 4c and d. As the sCO_2 releasing, the fluid transitions from a stagnant to a flowing state. A portion of the intrinsic energy is converted into expansion work performed by the outflowing fluid, leading to a reduction in the internal energy and temperature of the remaining fluid in the tank. For the same pressure drop, a lower initial pressure results in a longer discharge duration and lower rates of pressure and temperature change, allowing more working fluid to be released. Nevertheless, the total released mass only accounts for 5.2%–10.5% of the initial stored mass (see Fig. 5). A substantial amount of sCO_2 remains in the tank after discharge, rendering it unusable and limiting the improvement of ESD. Therefore, increasing the released mass is crucial for improving the ESD of the CCES systems.

2. Regenerated pressure storage tank

In classical thermodynamic theory, fluids above the critical point are regarded as a homogeneous phase, and their state is uniquely determined by temperature and pressure. However, analysis of fluid thermophysical properties indicates that, in the vicinity of a characteristic temperature, the isobaric specific heat c_p attains a maximum [30], as observed for CO_2 in Fig. 6a. This temperature is defined as the pseudo-critical temperature T_{pc} [30]. Around T_{pc}, the fluid density ρ also exhibits significant variation. When a supercritical fluid is heated and crosses the T_{pc}, part of the absorbed heat raises the fluid temperature (sensible heat), while another part increases the intermolecular spacing (latent heat). This behavior resembles a subcritical phase change process [31]. Based on this property, the "pseudo-phase transition theory" was introduced [31]. It has been validated in many previous studies and has been widely used to guide the design of sCO_2 heat exchangers [32,33]. Generally, supercritical fluids with temperatures below T_{pc} are termed liquid-like (high density), while those above T_{pc} are gas-like (low density). The region around T_{pc}, where density changes sharply, is referred to as the two-phase-like region. The boundary temperature between liquid-like and two-phase-like is denoted as T_-, and the boundary temperature between two-phase-like and gas-like is T_+ [34], as illustrated in Fig. 6a.

In Fig. 6b, three $T \sim P$ relations for different operating pressures of Fig. 4b are depicted. The discharge curve at an initial pressure of 10 MPa is closer to the $T_{pc} \sim P$ curve, whereas those at 15 MPa and 20 MPa deviate significantly. According to the "pseudo-phase transition theory" [31], $\Delta\rho$ reaches its maximum near T_{pc}. The released mass Δm is directly proportional to the density variation $\Delta\rho$. Thus, the case of 10 MPa exhibits superior discharge characteristics for released mass and duration. It can be inferred that to further enhance performance, the discharge curve of H-PST should approach or even cross the $T_{pc} \sim P$ curve (as blue dashed line in Fig. 6c). In this case, the working fluid undergoes full expansion, significantly increasing the released mass. However, without intervention, the fluid temperature decreases during expansion (as shown in Fig. 4d), preventing the discharge curve from approaching the $T_{pc} \sim P$ curve, and resulting in a smaller released mass. To mitigate the temperature decrease, this work proposes a regenerated pressure storage tank, which incorporates heat storage material (HSM) inside the constant-volume tank. The heat stored in the HSM is used to heat the sCO_2, thereby slowing its rate of temperature and pressure decrease and maximizing the density variation to achieve a larger released mass of sCO_2. The stored heat originates from the internal energy converted by the flow work of sCO_2 during the charging process and is released back to the sCO_2 during discharge, fully satisfying the laws of mass and energy conservation.

An HSM is integrated into the conventional PST to generate the R-PST, as shown in Fig. 7. The HSM improves the performance both in charging and discharging processes: During charging, the HSM absorbs internal energy of sCO_2 converted by flow work, reducing the rates of temperature and pressure increase, thus allowing more sCO_2 to be stored in the tank and enhancing storage capacity. During discharge, the HSM supplies heat to the sCO_2, reducing the temperature drop and thereby

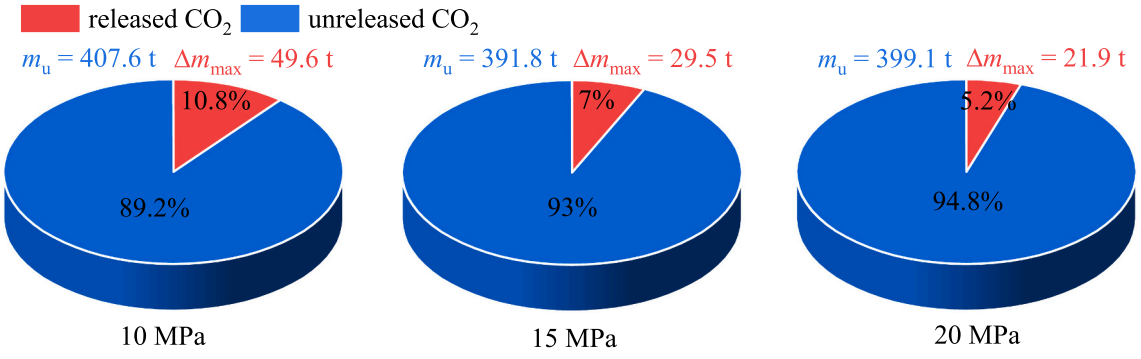


Fig. 5. The utilization rate of working fluid at initial pressures of 10, 15, and 20 MPa. m_u is the unreleased mass of CO_2. Δm_{max} is the total released mass of CO_2.

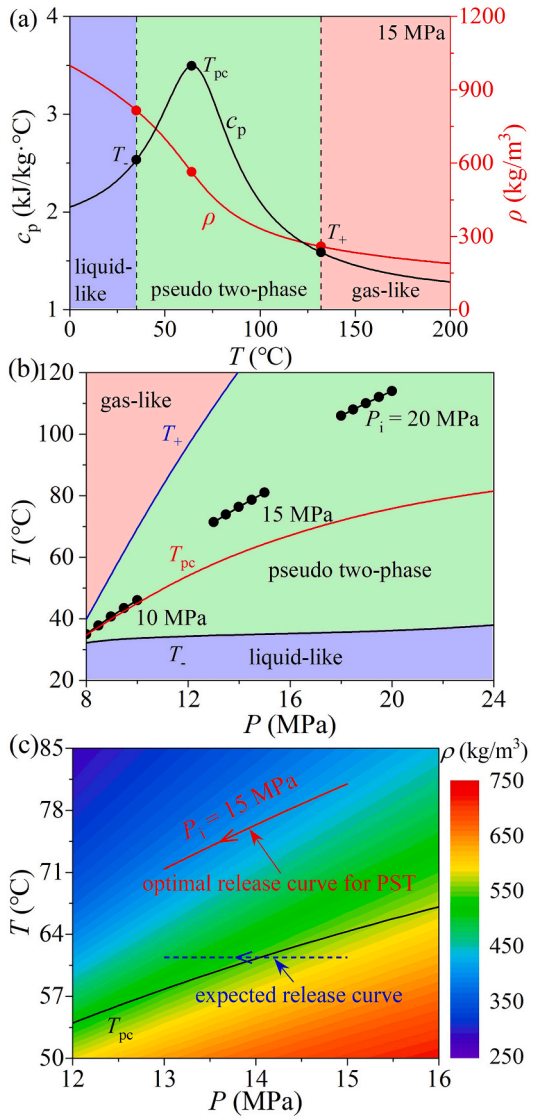


Fig. 6. The physical property of CO_2 (a is the specific heat c_p and density ρ versus temperature at 15 MPa. The supercritical CO_2 is divided into liquid-like state, pseudo two-phase, and gas-like state according to temperature. The boundary temperature between liquid-like and pseudo two-phase is denoted as T_-. The boundary temperature between pseudo two-phase and gas-like state is denoted as T_+. b displays the release curves for initial pressures of 10, 15, and 20 MPa in the CO_2 phase diagram. c shows the expected release curve, which fully exploits the rapid variation of the density in the vicinity of T_{pc}).

sustaining greater expansion capacity, which slows the rate of pressure decline while increasing the mass discharged. The incorporation of HSM reduces the pressure variation rate in both charging and discharging processes, improving the compressor and turbine operating stability.

2.1. The computational model and assumptions

For a better thermal performance, the HSM in R-PST should have a high surface area, high thermal conductivity, and large volumetric heat capacity. In this study, copper foam is selected as the HSM. The total tank volume is also maintained at 1000 m^3, identical to that of the conventional PST described in Section 1.1.

The first law of thermodynamics for the R-PST adds a heat storage term to Eq. (1), yielding:

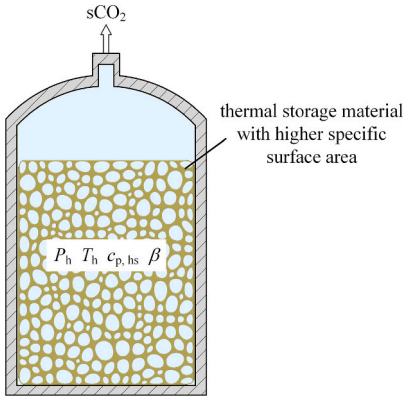


Fig. 7. Schematic diagram of a regenerative high-pressure tank (R-PST) for sCO_2.

$$Gu_c + m_c\frac{du_c}{dt} + \rho_{hs}V_{hs}c_{p,hs}\frac{dT_{hs}}{dt} = Gh_c \tag{5}$$

It is a differential form of the energy conservation equation, where ρ_{hs} is the density of HSM, V_{hs} is the volume of HSM, $c_{p,\,hs}$ is the specific heat at constant pressure of HSM, and T_{hs} is the temperature of the HSM. The first and second terms on the left-hand side of the equation represent the change rate of the internal energy of the sCO_2, while the third term denotes the variation rate of the internal energy of the HSM. The term on the right-hand side of the equation represents the energy flowing out of the tank, which contains the flow work.

The amount of heat transfer between the HSM and sCO_2 is expressed as:

$$Q' = hA(T_{hs} - T_h')t_s \tag{6}$$

where h is the convective heat transfer coefficient, A is the contact area between the HSM and sCO_2, T_h' is the temperature of sCO_2 before heat exchange between the HSM and sCO_2, and t_s is the time step. The intrinsic energy change of sCO_2 is given by:

$$Q'' = m_c(T_h''\text{-}T_h')\frac{c_v'' + c_v'}{2} \tag{7}$$

where c_v is the specific heat at constant volume of sCO_2, which is not constant but varies as a function of temperature T_h and pressure P_h of sCO_2. The superscripts "′" and "″" represent the states before and after heat exchange, respectively. To generalize the design for tanks of different sizes, the HSM volume fraction is introduced and defined as:

$$\beta = V_{hs}/V_h \tag{8}$$

The calculated procedure of the R-PST model is illustrated in Fig. 8. The pressure changes in the PST induced by the outflow of the sCO_2 propagate throughout the tank at the sonic velocity. For this study, the diameter of the spherical tank is ~12.4 m, and the sonic velocity of sCO_2 is about 360 m/s. Thus, the time required for the pressure to propagate from the outlet to the deepest point of the storage tank is approximately 34 ms, resulting in a near-instantaneous uniform pressure distribution within the tank. The pressure drop induces a corresponding temperature change of the sCO_2 throughout the entire tank, representing the conversion of thermal energy into flow work. Under non-transient, slow depressurization process, the sCO_2 in the PST is initially in thermal equilibrium and remains in thermal equilibrium throughout the gradual pressure release. Thus, the properties of CO_2 in PST are homogeneous. Now analyze the heat transfer between the HSM and sCO_2. The natural convection heat transfer coefficient h between the solid wall and sCO_2 is about 2 kW/m^{2}K [35], and the specific surface area of the copper foam is about 2000 m^2/m^3 [36]. Thus, for a unit volume, the heat-transfer capacity between sCO_2 and HSM is about 4×10^3 kW/K. During discharge

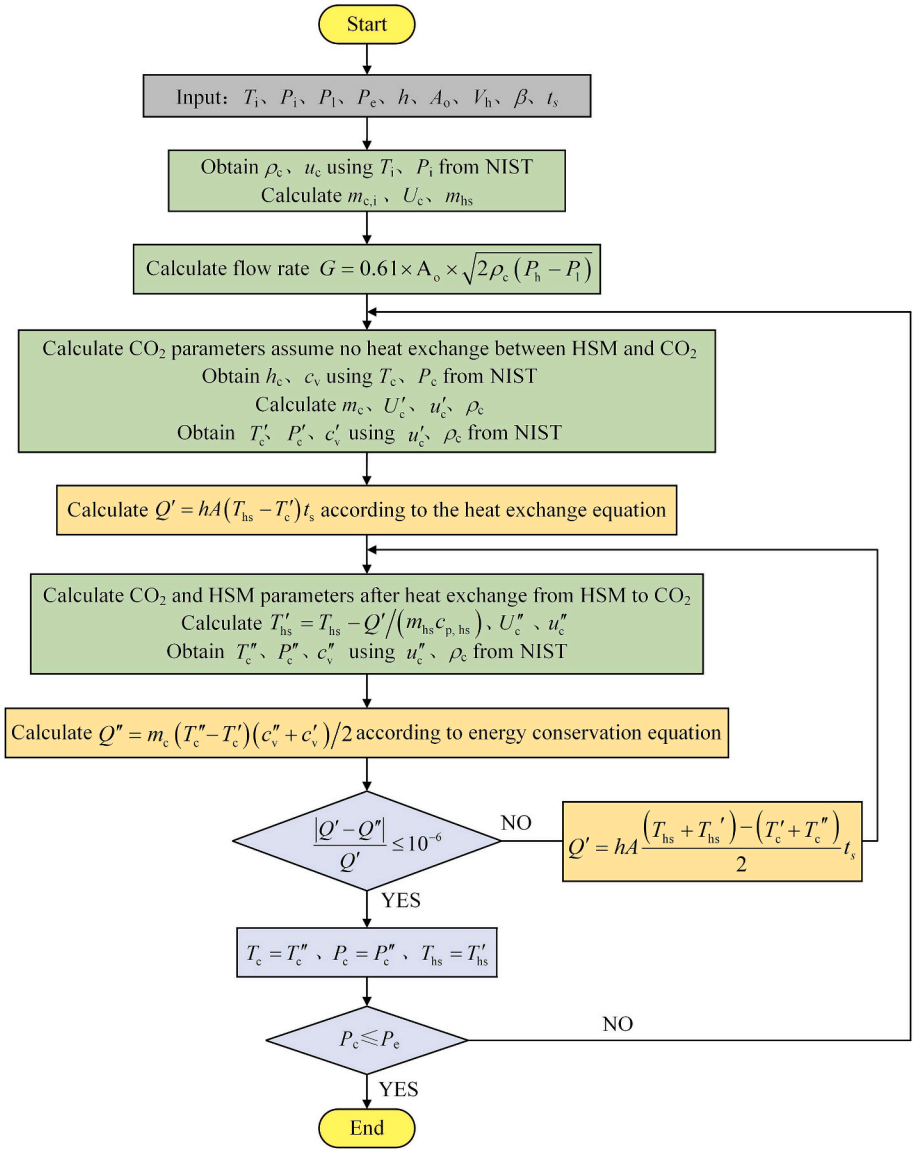


Fig. 8. Computational flowchart of the release process in a regenerative high-pressure tank.

process without HSM, the decrease in the internal energy of sCO_2 per second is about 1.7 kW per unit volume from the calculation above. One can get the temperature difference between HSM and sCO_2 is $\sim 4 \times 10^{-4}$ K. Therefore, heat can be transferred rapidly from the HSM to the sCO_2, and the near-instantaneous thermal equilibrium between them is reached (i.e., $T_{hs} = T_h''$). Since HSM is loosely and fully embedded in the PST, the sCO_2 is heated by the nearby HSM simultaneously everywhere. For copper foam, the Biot Number $Bi = hd_l/\lambda$ is about 0.01 with ligament thickness d_l of 2 mm and thermal conductivity λ = 400 W/(m·K). Therefore, the temperature difference within the HSM can also be neglected.

2.2. Discharge characteristics of the R-PST

A typical case with an initial pressure of 15 MPa is selected to analyze. The released mass Δm is calculated under various initial temperatures T_i and HSM fractions β, as shown in Fig. 9a. Δm exhibits an initial increase followed by a decrease as T_i and β increase, respectively (see Fig. 9b and c). The maximum released mass (46.4 t) occurs at T_i = 75 °C and β = 28%, which represents a 57.2% increase compared to the conventional PST of P_i = 15 MPa in Fig. 5. This means that the R-PST, utilizing only 82% of the volume, achieves 157.2% of the performance of the conventional PST operating at full (100%) volume. The optimal initial temperature is 5 °C lower than that of the conventional PST but still higher than T_{pc}. Thus, the discharge curve does not cross the $T_{pc} \sim P$ curve as expected in Fig. 6c. The finite heat capacity of copper foam cannot completely offset the cooling during expansion. Therefore, the optimal initial temperature of R-PST must be slightly higher than T_{pc} to ensure sufficient stored heat. For a fixed pressure and temperature, two inverse effects influence the performance of the R-PST as β increases: the thermal offset effect and the volume-occupying effect. At smaller β values, the mass release is dominated by the thermal offset effect. The heat released from the HSM compensates for expansion cooling and increases the discharged mass. Conversely, at larger β values, the reduced available fluid volume in R-PST lowers the total released mass. Hence, an optimal value of β must balance thermal storage in HSM and sCO_2 storage volume to maximize performance (as shown in Fig. 9c).

Figs. 10 and 11 analyze the influence of the HSM on the mass release characteristics of the R-PST. Fig. 10a presents the maximum released mass and its corresponding T_i for a R-PST at P_i = 15 MPa, across different HSM volume ratios β. As the β increases, the variation in the Δm_{max} is minimal within the β range of 20% to 40%. For practical applications, a

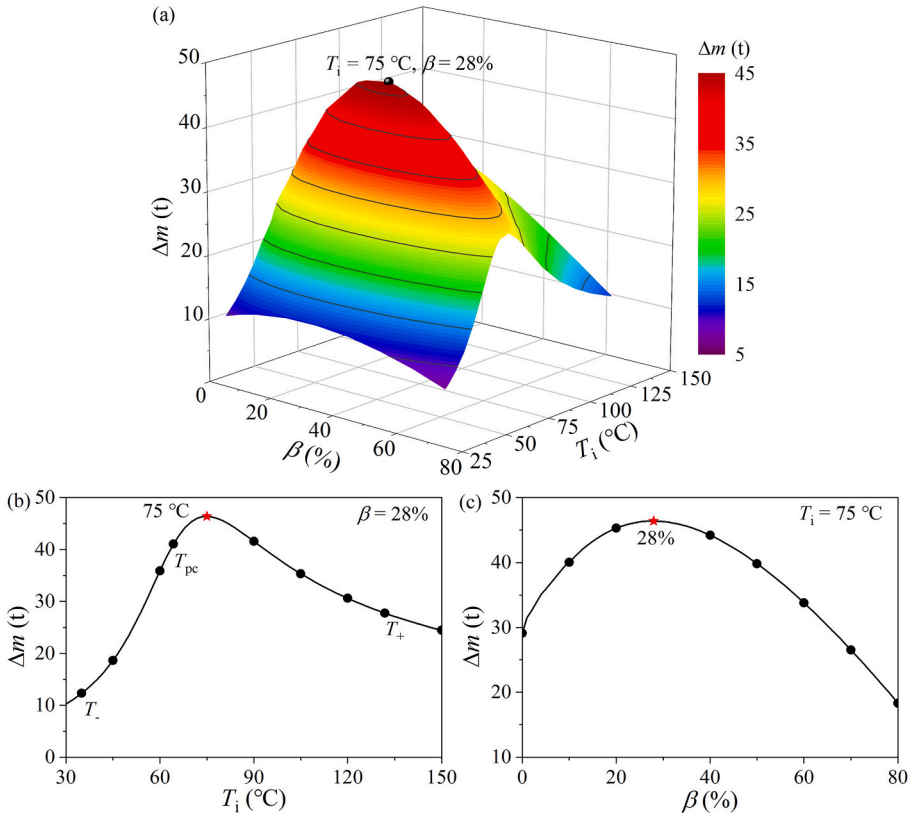


Fig. 9. Release characteristics of sCO_2 at an initial pressure of 15 MPa and work pressure difference of 2 MPa for R-PST. (a, The relationship between the released mass and the volume proportion of heat storage material, as well as the initial temperature. The largest released mass occurs at $T_i = 75$ °C and $\beta = 28\%$. b, The curve of released mass versus the initial temperature with $\beta = 28\%$. c, The curve of released mass versus the volume proportion of heat storage material with $T_i = 75$ °C.)

ratio of 20% can be selected to reduce the investment cost of the HSM. Furthermore, the optimal initial temperature T_i continuously decreases with increasing β. This offers two key advantages: 1) It enables a lower storage temperature T_i, which increases the mass storage volume of sCO_2 within the tank at a suitable β. 2) It reduces the temperature difference between the sCO_2 in R-PST and the ambient environment, thereby lowering insulation costs.

When the β is 28%, the mass flow rate G of the sCO_2 increases substantially, as illustrated in Fig. 10b. The density variation slope during the discharge process is significantly steeper for R-PST than for conventional PST ($\beta = 0$). The HSM enhances the expansion capability of the sCO_2. And the total released mass is increased by 16.9 t, and the discharge duration is extended by over 50%. This implies that the turbine in the CCES system can achieve higher power and a greater total work output. From the temporal evolution of pressure and temperature in Fig. 10c, the HSM reduces the required optimal initial temperature by 6 °C and slows the rates of temperature and pressure change. The temperature drop per unit pressure decrease is reduced from 4.00 °C/MPa to 2.32 °C/MPa, confirming that HSM effectively mitigates temperature decline during depressurization.

The above results demonstrate that the R-PST significantly enhances mass release and energy storage density of CCES systems. Although the HSM reduces the optimal initial temperature, the discharge curve does not cross the line of $T_{pc} \sim P$. Why does the HSM influence the discharge characteristics of R-PST in this manner? The mechanism is analyzed from the perspective of physical property variation. During the discharge process, the tank volume remains constant, and the change of sCO_2 density directly reflects the amount of released sCO_2 ($\Delta m = \Delta\rho V_h$). Throughout the entire discharge process, the density change of the sCO_2 inside the R-PST depends solely on its initial and final thermodynamic states and is therefore path-independent. However, the final state of the sCO_2 is determined by the initial condition and the boundary conditions of the release process. In other words, these initial and boundary conditions fully determine the density change of the sCO_2. In this study, for a given initial pressure and cut-off pressure, the initial condition is primarily determined by the initial temperature, while the boundary condition of the release process is characterized by the HSM volume fraction (β). Therefore, optimizing both the initial temperature and the HSM volume fraction can modify the discharge curves shown in Fig. 11 and maximize the releasable mass of the sCO_2 shown in Fig. 9a.

A larger density variation of sCO_2 within the storage tank leads to an increased amount of working fluid released during discharge. According to thermodynamic principles, the sCO_2 density is a function of pressure and temperature, which leads to the following differential relationship:

$$\Delta\rho = \frac{\partial\rho}{\partial P}\mathrm{d}P + \frac{\partial\rho}{\partial T}\mathrm{d}T = \left|\frac{\partial\rho}{\partial P}\right|\mathrm{d}P - \left|\frac{\partial\rho}{\partial T}\right|\mathrm{d}T \tag{9}$$

For sCO_2, the partial derivative of the pressure term $\partial\rho/\partial P$ is positive, while the temperature term $\partial\rho/\partial T$ is negative. This means that pressure variation acts as an excitation effect, whereas temperature acts as a punishing effect. For analytical clarity, the absolute values of these derivatives are considered. To maximize the overall density variation $\Delta\rho$, one must increase the pressure term and reduce the temperature term on the right-hand side of Eq. (9). Fig. 11a and b are the contour maps of the absolute values of the density partial derivatives with respect to pressure and temperature, respectively. The two characteristic curves of $|\partial\rho/\partial P|_{max}$ and $|\partial\rho/\partial T|_{max}$ lie on opposite sides of the line of $T_{pc} \sim P$. The influence of pressure on density variation is much stronger than that of temperature. Combining Eq. (9) and Fig. 11, increasing the pressure contribution requires the discharge curve to be as close as possible to the curve $|\partial\rho/\partial P|_{max}$ and to have a large pressure drop. Conversely, minimizing the temperature contribution requires the curve to be farther

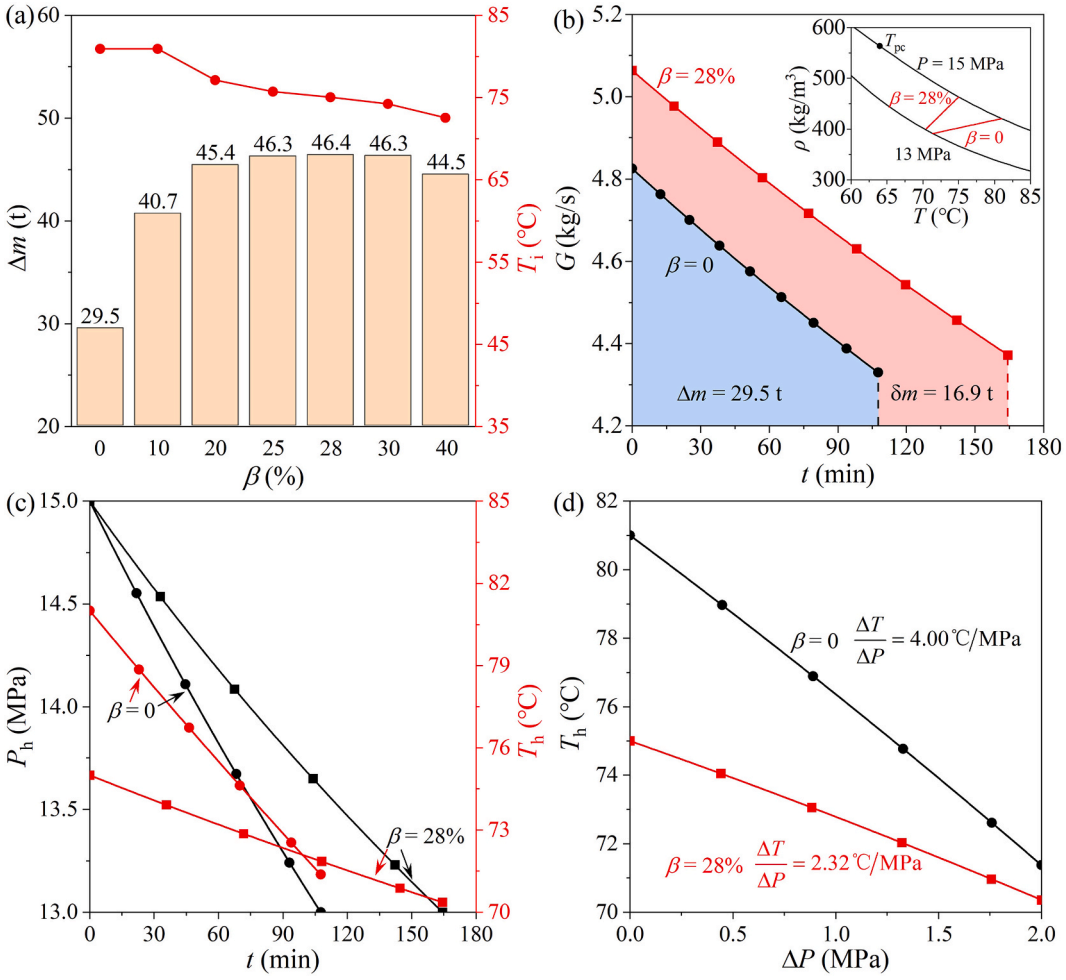


Fig. 10. The comparison of optimal sCO_2 release characteristics: PST vs. R-PST ($P_i = 15$ MPa, $\Delta P = 2$ MPa) (a, the optimal sCO_2 released mass and initial temperature at different volume proportion β of heat storage material. b, the curves of mass flow rate G versus time for $\beta = 0$ and $\beta = 28\%$ at optimal initial temperature. The inset figure is the density variations for the release process at $\beta = 0$ and $\beta = 28\%$. c, The curves of pressure and temperature versus time for $\beta = 0$ and $\beta = 28\%$. d, the curves of temperature versus pressure variation during the R-PST release process for $\beta = 0$ and $\beta = 28\%$).

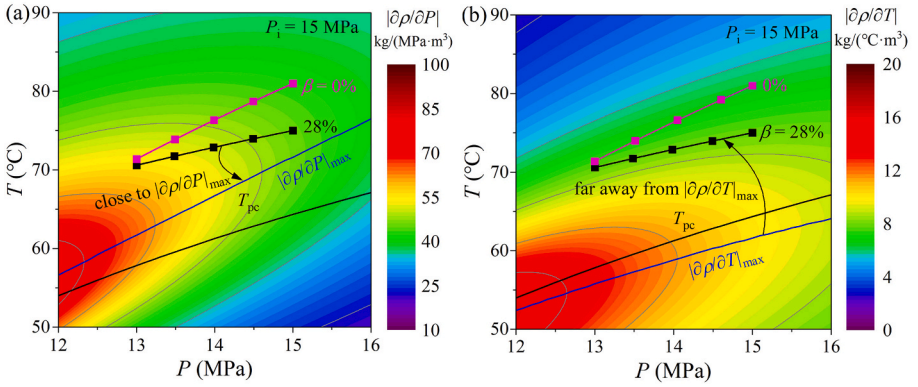


Fig. 11. The map of the partial derivative of density with respect to pressure and temperature. Subfigures a and b are for $|\partial\rho/\partial P|$ and $|\partial\rho/\partial T|$, respectively.

from the curve $|\partial\rho/\partial T|_{max}$ and to maintain a small temperature change. To satisfy both conditions simultaneously, the optimal discharge curve should lie above $T_{pc} \sim P$. The introduction of HSM suppresses temperature variation inside the tank, thereby weakening the temperature-induced penalty effect and allowing the discharge path to approach the ideal curve.

3. Sensitivity analysis

In the above sections, a typical case with $P_i = 15$ MPa, a working pressure differential $\Delta P = 2$ MPa, and copper-foam as HSM was used to study the effect of HSM on the performance of the tank discharge process. A control variate method was used to analyze the effect of initial pressure P_i, working pressure differential ΔP, and HSM thermophysical

properties on the performance of R-PST, which delineates the applicability range of the R-PST.

3.1. The effect of initial pressure P_i

Keeping the $\Delta P = 2$ MPa, the influence of the initial pressure P_i on R-PST discharge performance is studied. As the P_i increases, the optimal HSM volume fraction β that maximizes released mass decreases, while the optimal T_i rises (Fig. 12a). At relatively low P_i, the HSM can substantially increase the released mass; however, as the P_i grows, the benefit of HSM on increasing mass release diminishes. The relative gain in released mass due to HSM falls from 124.7% to 19.0% (Fig. 12b). This trend is mainly attributable to the reduction of the density gradient $\partial\rho/\partial T$ with increasing pressure: at higher pressures, sCO_2 density is less sensitive to temperature changes but sensitive to pressure, so the same amount of heat supplied by the HSM produces a smaller increment in sCO_2 expansion and thus a smaller increase in released mass. Moreover, increasing β reduces the free volume available for sCO_2 storage, which can offset or even reverse the mass-release benefit at high β. Thus, the optimal β decreases as initial pressure increases.

Although the R-PST may not outperform conventional PST in terms of released mass at high P_i, it can markedly reduce the required T_i, as shown in Fig. 13. Here, the released mass is fixed to the maximum value obtainable by the conventional PST at the corresponding initial pressure. With increasing P_i, the optimal HSM fraction β decreases, but the difference of T_i between the R-PST and conventional PST increases. The higher P_i, the greater the reduction in required T_i induced by the HSM. For example, at $P_i = 30$ MPa, the reduction of required T_i of the R-PST is about 36% (~62 °C) compared to the conventional PST. This temperature reduction is advantageous for CCES operation. The higher P_i typically corresponds to higher T_i (which increases thermal losses to the environment and reduces system efficiency), the R-PST can achieve the same released mass at a substantially lower T_i. This reduces insulation demands and associated costs for the storage tank while preserving or improving usable energy release.

3.2. The effect of working pressure differential ΔP

The working pressure differential ΔP is the pressure difference between the initial pressure T_i and the terminal pressure P_e of the PST. According to Eq. (9), the working pressure differential ΔP exerts a significant influence on the thermodynamic behavior of the R-PST. Taking initial pressures of 15 MPa and 20 MPa as the typical cases, the effects of ΔP on the released mass are analyzed. The corresponding variations in optimal T_i and HSM volume fraction β are shown in Fig. 14a–d. As ΔP increases, the optimal HSM fraction β first increases and then decreases, while the optimal initial temperature T_i continuously decreases. Compared with the conventional PST, the performance advantage of the R-PST (in terms of released mass) becomes increasingly pronounced at larger ΔP. When the pressure differential ΔP is small, this pressure drop range restricts sCO_2 expansion that benefits from pressure variation. It is preferable to operate at a higher T_i with a smaller $|\partial\rho/\partial T|$, and a moderately low HSM fraction β to compensate for cooling losses. However, for a larger pressure differential ΔP, the sCO_2 expansion induced by pressure variation is considerable. Maintaining a high released mass demands a lower initial temperature T_i to increase stored CO_2 mass in R-PST and a higher HSM fraction to supply sufficient heat and suppress the punishing effect of temperature reduction.

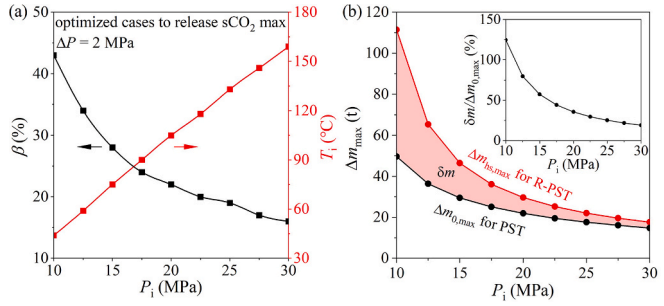


Fig. 12. The effect of initial pressure on release characteristic for R-PST (a, the curves of optimal volume proportion β of heat storage material and initial temperature versus initial pressure. b, the comparison of the optimal released mass between R-PST and PST at different initial pressures. Inset: percentage increase of R-PST vs. PST at different initial pressures. The $\Delta m_{hs,\ max}$ is the optimal released mass of the R-PST. The $\Delta m_{0,\ max}$ is the optimal released mass for PST. The δm is the difference between $\Delta m_{hs,\ max}$ and $\Delta m_{0,\ max}$ at the same pressure).

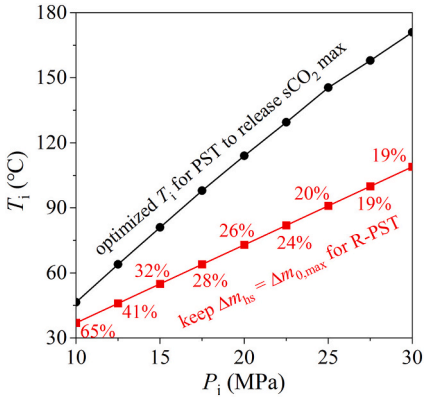


Fig. 13. R-PST decreases the required initial temperature compared to PST, with the released mass Δm_{hs} being equal to the optimal released mass $\Delta m_{0,max}$ of PST.

Fig. 14e–f illustrate the discharge curves for $P_i = 15$ MPa under different ΔP in the contour maps of the $|\partial\rho/\partial P|$ and $|\partial\rho/\partial T|$. With increasing pressure differential ΔP, the discharge curve shifts downward toward the curves of $|\partial\rho/\partial P|_{max}$, indicating that the fluid state moves closer to the pseudo-critical region where density is more sensitive to pressure variation. In particular, at $\Delta P = 7$ MPa, the later stage of discharge exhibits a high $|\partial\rho/\partial P|$. The pressure variations dominate the density change. And, the influence of temperature variation is relatively weaker. As a result, the demand for heat compensation from the HSM decreases. In addition, an overly large HSM fraction would undesirably reduce the CO_2 storage volume in this stage. Consequently, as ΔP increases, the optimal HSM fraction β first increases and then decreases, balancing the need for sufficient heat storage in the HSM with the requirement to maximize the stored volume of sCO_2.

3.3. The effect of HSM thermophysical properties

The previous analyses were based on copper foam as the HSM. It is obvious that the thermophysical properties of the HSM play a crucial role in determining both the optimal discharge parameters and the mass of released sCO_2 in the R-PST. The heat compensation capacity of the HSM is closely related to its heat exchange capability, given by:

$$Q = \rho_{hs} c_{p,hs} V_{hs} \frac{dT_{hs}}{dt} = \xi V_{hs} \frac{dT_{hs}}{dt} \tag{10}$$

where $\xi = \rho_{hs} c_{p,hs}$ represents the volumetric heat capacity, which characterizes the HSM's ability to store and release heat per unit volume.

The effects of volumetric heat capacity on the discharge characteristic of R-PST were analyzed at $P_i = 15$ MPa, $\Delta P = 2$ MPa, and $\beta = 28\%$ (see Fig. 15). Here, $\xi = 0$ corresponds to a material that merely occupies tank volume without contributing heat, and an infinitely large ξ implies isothermal discharge. As ξ increases, both the discharged mass and discharge rate of the sCO_2 rise significantly. Under isothermal discharge,

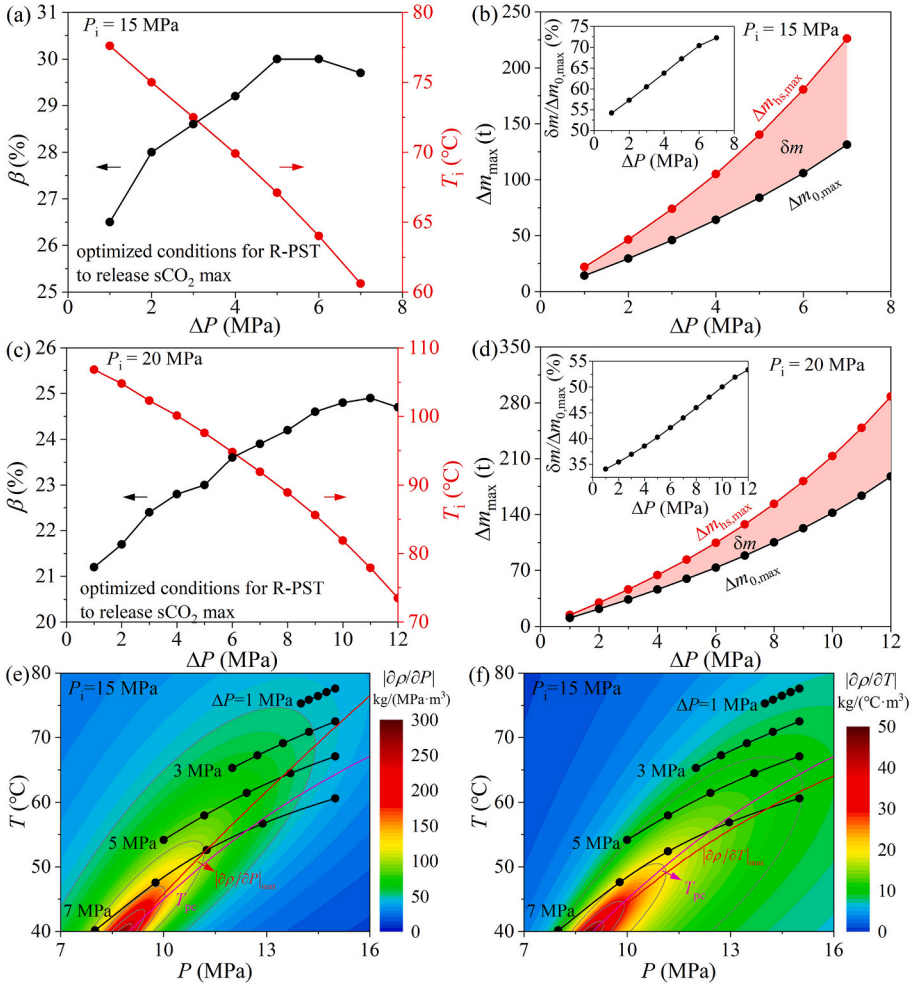


Fig. 14. The effect of work pressure difference ΔP on release characteristic of R-PST (a, the curves of optimal β and T_i versus ΔP at $P_i = 15$ MPa. b, the comparison of optimal released mass Δm_{max} between R-PST and PST at different ΔP for $P_i = 15$ MPa. Inset: percentage increase of R-PST vs. PST at different ΔP. The $\Delta m_{hs,\ max}$ is the optimal released mass of the R-PST. The $\Delta m_{0,\ max}$ is the optimal released mass for PST. The δm is the difference between $\Delta m_{hs,\ max}$ and $\Delta m_{0,\ max}$ at the same pressure. c, the curves of optimal β and T_i versus ΔP at $P_i = 20$ MPa. d, the comparison of optimal released mass between R-PST and PST at different ΔP for $P_i = 15$ MPa. Inset: percentage increase of R-PST vs. PST at different ΔP. e and f show the release curves at different ΔP values in the map of the partial derivative of density with respect to pressure and temperature for $P_i = 15$ MPa).

the usage rate of sCO_2 reaches 19.59%, compared with only 7% for the conventional PST. In Fig. 15a–b, the effect of different HSMs on the performance of R-PST was compared. The usage rate of sCO_2 was above 12% for all HSMs. Among sensible heat storage materials, water exhibits the highest volumetric heat capacity (4200 kJ/m^3·°C), yielding a released mass of 49.0 t. For phase change materials (PCMs), sodium acetate trihydrate ($CH_3COONa·3H_2O$) outperforms paraffin, achieving 50.4 t of released mass due to its higher volumetric heat capacity. Fig. 15c–d show the discharge characteristics of R-PST with different HSMs. It should be noted that although aligning the discharge curve exactly with the $|\partial\rho/\partial P|_{max}$ curve maximizes the pressure term in Eq. (9), this does not correspond to the overall optimal condition because the temperature term's penalizing effect persists. As the volumetric heat capacity ξ increases, the slope of the discharge curve decreases, indicating reduced temperature variation and weakened penalization from the temperature term. Consequently, the discharge curve moves closer to the $|\partial\rho/\partial P|_{max}$ curve. Under isothermal discharge, the temperature effect disappears entirely, allowing the trajectory to fully cross the $|\partial\rho/\partial P|_{max}$ curve and maximize the expansion effect driven by pressure reduction.

From the sensitivity analysis above, the performance of the R-PST is superior to that of the conventional PST under all conditions. The R-PST is preferred for the CCES system employing a PST with relatively low initial pressure and a large working pressure differential. Under the conditions of higher initial pressures, the R-PST also proves beneficial for reducing the storage temperature. Moreover, HSMs with higher volumetric heat capacity further enhance the performance of the R-PST. An optimized HSM volume fraction β is required to balance the need for sufficient heat storage with the demand to maximize the stored volume of sCO_2.

4. Operational characteristics of CCES coupling R-PST

Here, the CCES system presented in Reference [26] is adopted as the benchmark case to examine the operational characteristics of the R-PST within a practical CCES configuration, in which the dynamic behaviors of the CCES system during the energy-storage and release processes are investigated. The system configuration is identical to that shown in Fig. 2, and the model assumptions and detailed system parameters are consistent with those in Reference [26]. Dynamic models of the turbine, compressor, heat exchangers, and pressure-storage tank are provided in the supplementary material. It should be noted that the dynamic model of the PST in Reference [26] is identical to that employed in this work. The design condition defined in Reference [26] is selected as the base operating condition. For the CCES system coupled with the R-PST, only Eq. (5) is used to replace the original model of PST. The H-PST of the

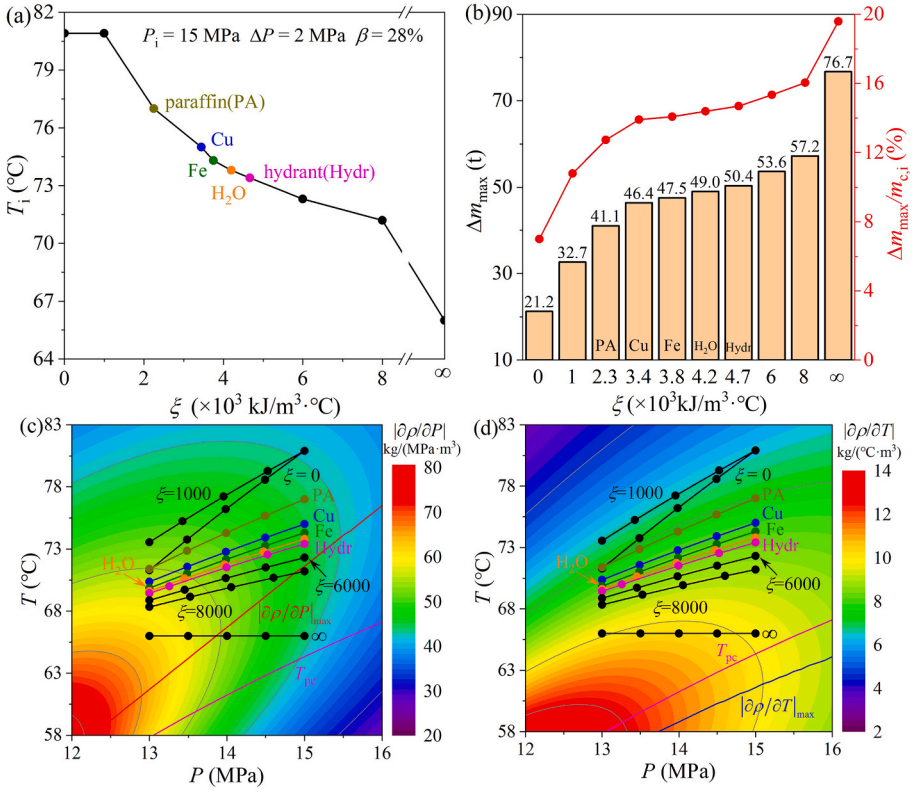


Fig. 15. The effect of volumetric heat capacity ξ on release characteristic for R-PST (a, the curves of optimal T_i versus ξ at $P_i = 15$ MPa, $\Delta P = 2$ MPa, and $\beta = 28\%$. b, the effect of volumetric heat capacity on the optimal Δm and percentage increase of R-PST vs. PST. c and d show the release curves at different ξ values in the map of the partial derivative of density with respect to pressure and temperature).

CCES adopts R-PST, and L-PST is still the conventional PST. The HSM volume fractions β is 20%, and HSM is assumed to be in thermal

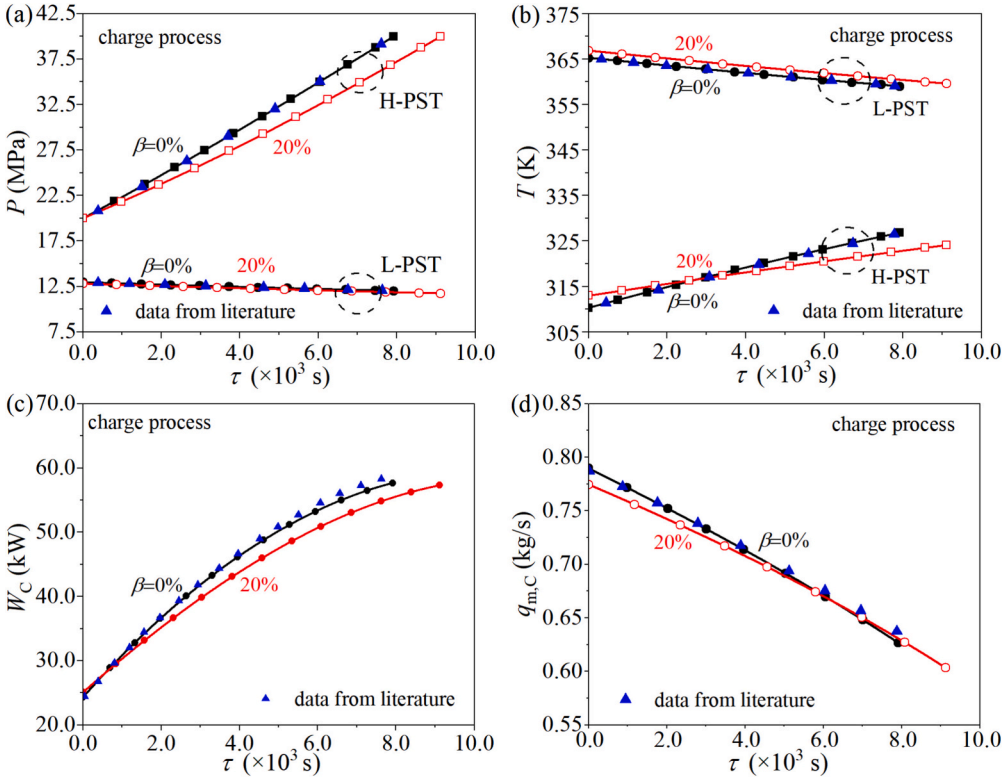


Fig. 16. The dynamic characteristics of the charging process (a, changes in the L-PST and H-PST pressure; b, changes in the L-PST and H-PST temperature; c, the dynamic characteristics of the compressor for benchmark case (β = 0%) and case with HSM (β = 20%), respectively; d, the mass flow rate of the compressor).

equilibrium with the sCO_2. All other model assumptions and parameter settings remain consistent with those in Reference [26].

The dynamic characteristics of the CCES systems during the charging process are illustrated in Fig. 16. The case of $\beta = 0$ represents the base operation, and the calculated results agree well with those reported in Reference [26]. The case of $\beta = 20\%$ corresponds to the CCES system coupled with the R-PST. As shown in Fig. 16a and b, embedding the HSM inside the H-PST effectively suppresses the rate of pressure and temperature rise during charging process. Since the L-PST does not contain an HSM, both the baseline and R-PST coupled cases exhibit nearly identical variations. Fig. 16c presents the variation of compressor power. Coupling the R-PST moderates the power rise rate and extends the operation time, primarily because the HSM slows the pressure increase in the H-PST, thereby prolonging the charging process. The corresponding sCO_2 mass-flow evolution through the compressor is shown in Fig. 16d. For the base case, the compressor consumes 346.49 MJ of work to compress a total of 5.64 t of sCO_2. In comparison, for the CCES system coupling R-PST, the compression work and flow mass are 398.15 MJ and 6.34 t, representing increases of 14.9% and 12.4%, respectively. These results indicate that the R-PST enhances both the sCO_2 storage capacity and the overall compressor energy input during charging.

The dynamic characteristics of the CCES systems during the discharging process are shown in Fig. 17. The baseline results again match those given in Reference [26]. Fig. 17a and b depict the pressure and temperature variations in the H-PST and L-PST. Consistent with the previous findings, the R-PST effectively reduces the rates of pressure and temperature drop rate during discharging. Fig. 17c shows the turbine power variation obtained from the dynamic model. The R-PST increases the turbine's power output and mitigates the decline rate during the discharge process. The evolution of the mass-flow rate from the H-PST is shown in Fig. 17d, confirming that the R-PST promotes a greater sCO_2 release. Over the entire discharge period, the turbine expansion work for the baseline case is 214.46 MJ, with 5.64 t of sCO_2 released. For the R-PST coupled CCES system, the expansion work and released mass reach 247.53 MJ and 6.34 t, corresponding to increases of 15.4% and 12.4%, respectively. Based on above results, the energy-storage efficiency and the ESD of the base case are 61.87% and 429 kJ/m^3, respectively, while the R-PST coupled configuration slightly enhances the efficiency to 62.17% and raises the ESD to 494.87 kJ/m^3, representing a 15.3% improvement. In summary, integrating the R-PST could significantly increase the sCO_2 release from the PST, thereby enhancing the net power output and ESD of the CCES system.

5. Limitations and prospects

This study is entirely numerical and is developed based on the lumped-parameter method and thermodynamic equations. Several significant simplifications were adopted in the modeling process. The validation shown in Fig. 3 only verifies the correctness of the storage tank model of conventional PST and the numerical approach. As for R-PST, the thermal coupling between the proposed HSM and the sCO_2 in the tank is derived from heat transfer theory and energy balance equations. Time-scale and dimensionless analyses further demonstrate the feasibility of heat exchange between copper foam and sCO_2. The computational model of the R-PST was developed by modifying the conventional storage tank model. As no relevant studies are currently available, there are no experimental or numerical data for direct comparison. From a theoretical analysis, the proposed thermal coupling between the HSM and sCO_2 can effectively enhance CO_2 release. However, the present R-PST remains a thermodynamics-based conceptual model. To further substantiate its validity, both experimental investigations and CFD simulations are necessary to study the actual heat coupling process between the HSM and sCO_2, as well as to analyze how the internal flow behavior affects the temperature distribution within the tank. Section 4 has already demonstrated that employing the R-PST significantly improves the performance of the CCES system, leading to higher energy storage density and net output work. Future studies should conduct an in-depth analysis of the CCES dynamic characteristics

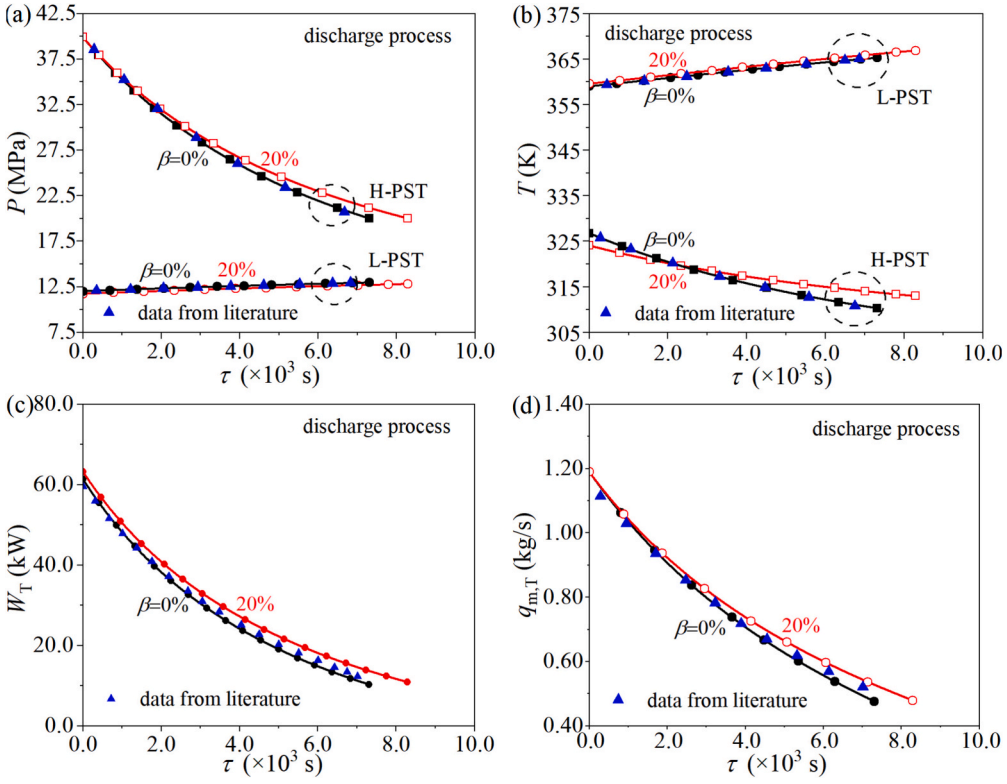


Fig. 17. The dynamic characteristics of the discharging process (a, changes in the L-PST and H-PST pressure; b, changes in the L-PST and H-PST temperature; c, the dynamic characteristics of the turbine for benchmark case ($\beta = 0\%$) and case with HSM ($\beta = 20\%$), respectively; d, the mass flow rate of the turbine).

coupling the R-PST, examine the influence of different operating factors on system performance, and establish guidelines for optimal design.

In engineering applications, the HSM is loosely embedded in the PST. The HSM must demonstrate excellent thermal performance while also ensuring compatibility with sCO_2, manufacturability, durability, cost-effectiveness, and practical ease of installation and maintenance. Iron is unsuitable as a HSM because it can react with sCO_2 in the presence of trace moisture, leading to corrosion [37]. Although water and sodium acetate trihydrate exhibit outstanding thermal compensation and discharge performance (as shown in Fig. 15b), their use requires complex encapsulation and heat exchange structures, which increase manufacturing difficulty and overall cost. Considering these factors comprehensively, copper foam emerges as the most favorable option. Copper provides superior thermal conductivity and does not react with sCO_2. Moreover, its porous foam structure significantly enhances the specific surface area, thereby improving overall heat transfer performance. Because the temperature variation of sCO_2 during charging and discharging is relatively small ($\sim$ 20 °C), the associated volumetric change of the HSM is negligible. The copper foam can simply be placed and secured inside the tank without affecting the structural integrity of the vessel. While incorporating the HSM into the PST increases initial construction costs, it also improves the ESD of the CCES system without adding operating expenses. This is a one-time investment with no subsequent maintenance requirements, thereby contributing positively to the system's overall economic performance.

6. Conclusions

This study introduces a novel PST with built-in thermal storage material to address the low usage efficiency of sCO_2 in conventional PST of CCES systems. The mass release characteristics of R-PST and conventional PST are systematically investigated through comprehensive modeling, simulation, and parameter analysis. The main findings are as follows:

1. A PST with built-in thermal storage material was proposed to overcome the poor utilization of sCO_2. Using copper foam as the HSM, the R-PST substantially increases mass flow rate and mass usage fraction. As HSM volume fraction β and the initial temperature T_i increase, the total released mass first grows and then declines. For $P_i = 15$ MPa, the optimal parameters are $\beta = 28\%$ and $T_i = 75$ °C, yielding a released mass approximately 57.2% higher than that of the conventional PST.
2. From the perspective of energy, during discharge, the stored heat is compensated to the sCO_2, replenishes the sCO_2 internal energy lost during expansion, thereby moderating its pressure drop. From physical property insight, incorporating the HSM mitigates temperature variation inside the tank, reducing the density variation associated with temperature change, improving mass release.
3. The effects of initial pressure P_i, working pressure differential ΔP, and HSM volumetric heat capacity ξ were systematically analyzed. As the P_i increases, the incremental benefit of the HSM on released mass gradually diminishes. Nonetheless, at high pressures, the HSM enables a significantly lower required optimal initial temperature of $\sim$60 °C, relaxing insulation demands on the tank. Increasing ΔP shifts the optimal T_i to a lower value and further raises the released mass. Materials with higher volumetric heat capacity markedly improve released mass.
4. Under realistic turbine and compressor modeling, the R-PST coupled CCES exhibits a 15.3% increase in ESD, reaching 494.87 kJ/m^3, with the corresponding efficiency improved to 62.17%, compared to the base configuration without R-PST for the same design parameters.

In summary, the R-PST is an effective strategy to enhance the CO_2 mass release and the energy storage density of CCES, offering a practical and scalable pathway for improving thermal management, system efficiency, and engineering applicability of next-generation supercritical CCES.

CRediT authorship contribution statement

Xin Yan: Writing – review & editing, Writing – original draft, Supervision, Project administration, Funding acquisition, Conceptualization. **Lulu Xing:** Writing – review & editing, Investigation. **Yuqian Zhang:** Investigation. **Jinliang Xu:** Supervision, Funding acquisition. **Rui Wu:** Data curation. **Helong Su:** Data curation.

Declaration of competing interest

The authors declare no competing financial interest.

Acknowledgements

The authors acknowledge the support from the National Natural Science Foundation of China (52306195 and 52130608).

Appendix A. Supplementary data

Supplementary data to this article can be found online at https://doi.org/10.1016/j.est.2026.123289.

Data availability

Data will be made available on request.

References

[1] Y. Yang, L. Tong, Y. Liu, et al., A novel integrated system of hydrogen liquefaction process and liquid air energy storage (LAES): energy, exergy, and economic analysis, Energy Convers. Manag. 280 (2023) 116799.
[2] Y. Lu, X. Yang, D. Bian, et al., A novel approach for quantifying water resource spatial equilibrium based on the regional evaluation, spatiotemporal heterogeneity and geodetector analysis integrated model, J. Clean. Prod. 424 (2023) 138791.
[3] K. Chen, M. Pan, Operation optimization of combined cooling, heating, and power superstructure system for satisfying demand fluctuation, Energy 237 (2021) 121599.
[4] W. Wang, B. Yuan, Q. Sun, et al., Application of energy storage in integrated energy systems — a solution to fluctuation and uncertainty of renewable energy, J. Energy Storage 52 (2022) 104812.
[5] G. Olabi A, T. Wilberforce, M. Ramadan, et al., Compressed air energy storage systems: components and operating parameters – a review, J. Energy Storage 34 (2021) 102000.
[6] H. Jafarizadeh, M. Soltani, J. Nathwani, Assessment of the Huntorf compressed air energy storage plant performance under enhanced modifications, Energy Convers. Manag. 209 (2020) 112662.
[7] P. Holden, D. Moen, M. Decorso, et al., Alabama electric cooperative compressed air energy storage (CAES) plant improvements, in: Proceedings of the ASME Turbo Expo 2000: Power for Land, Sea, and Air, F, 2000. V003T02A021.
[8] X. Zhang, Z. Gao, B. Zhou, et al., Advanced compressed air energy storage systems: fundamentals and applications, Engineering 34 (2024) 246–269.
[9] X. Liu, K. Wang, Q. He, Compressed carbon dioxide energy storage: a comprehensive review of principles, research progress and prospects, Energy 324 (2025) 136028.
[10] S. Liu, S. Wu, Y. Hu, et al., Comparative analysis of air and CO_2 as working fluids for compressed and liquefied gas energy storage technologies, Energy Convers. Manag. 181 (2019) 608–620.
[11] L. Sun, B. Tang, Y. Xie, Performance assessment of two compressed and liquid carbon dioxide energy storage systems: thermodynamic, exergoeconomic analysis and multi-objective optimization, Energy 256 (2022) 124648.
[12] Y. Guo, J. Xu, X. Yu, et al., Optimization of dynamic compressed CO_2 energy storage system: the role of supercritical fluid properties, Energy 328 (2025).
[13] Lexuan Li Y X, Yin Zhao, Guo Huan, Zhang Xianrong, Chen Haisheng, Zhou Xuezhi, Exergy destruction characteristics of a supercritical carbon-dioxide energy storage system, Energy Storage Sci. Technol. 10 (5) (2021) 1824–1834.
[14] B. Stanek, J. Ochmann, Ł. Bartela, et al., Isobaric tanks system for carbon dioxide energy storage – the performance analysis, J. Energy Storage 52 (2022) 104826.
[15] M. Xu, X. Wang, Z. Wang, et al., Preliminary design and performance assessment of compressed supercritical carbon dioxide energy storage system, Appl. Therm. Eng. 183 (2021) 116153.
[16] H. Liu, Q. He, A. Borgia, et al., Thermodynamic analysis of a compressed carbon dioxide energy storage system using two saline aquifers at different depths as storage reservoirs, Energy Convers. Manag. 127 (2016) 149–159.

[17] P. Zhao, W. Xu, F. Gou, et al., Performance analysis of a self-condensation compressed carbon dioxide energy storage system with vortex tube, J. Energy Storage 41 (2021) 102995.
[18] M. Astolfi, D. Rizzi, E. Macchi, et al., A novel energy storage system based on carbon dioxide unique thermodynamic properties, J. Eng. Gas Turbines Power 144 (8) (2022).
[19] Y. Zhou, Y. Huang, G. Tian, et al., Classification and characteristics of supercritical carbon dioxide leakage from a vessel, Energy 258 (2022) 124790.
[20] Z. Liu, H. Guan, J. Shao, et al., Thermodynamic and advanced exergy analysis of a trans-critical CO_2 energy storage system integrated with heat supply and solar energy, Energy 302 (2024) 131507.
[21] Z. Liu, H. Guan, X. Jin, et al., Thermodynamic and economic analysis of a trans-critical CO_2 energy storage system integrated with ORC and solar energy, Energy 313 (2024) 133667.
[22] A. Sciacovelli, Y. Li, H. Chen, et al., Dynamic simulation of Adiabatic Compressed Air Energy Storage (A-CAES) plant with integrated thermal storage – link between components performance and plant performance, Appl. Energy 185 (2017) 16–28.
[23] B. Cardenas, S. Garvey, J. Rouse, et al., Design of a combined heat store and heat exchanger for CAES systems, IET Renew. Power Gener. 19 (1) (2025) e70064.
[24] E. Barbour, D. Mignard, Y. Ding, et al., Adiabatic Compressed Air Energy Storage with packed bed thermal energy storage, Appl. Energy 155 (2015) 804–815.
[25] B. Cárdenas, S. Garvey, A directly charged thermal store for compressed air energy storage systems, J. Energy Storage 71 (2023) 108183.
[26] J. Jiang, B. Zhang, W. Chen, et al., Investigation and optimization of the thermal performance of compressed supercritical CO2 energy storage system based on dynamic modeling and transient simulation, Renew. Energy 238 (2025) 121966.
[27] S. Vemulapalli, K. Venkata S, Parametric analysis of orifice plates on measurement of flow: a review, Ain Shams Eng. J. 13 (3) (2022) 101639.
[28] E. Lemmon, M. Huber, M. Mclinden, NIST Standard Reference Database 23: Reference Fluid Thermodynamic and Transport Properties-REFPROP, Version 9.1, NIST, 2013.
[29] F. Xiao, W. Chen, B. Zhang, et al., A novel constant power operation mode of constant volume expansion process for AA-CAES: regulation strategy, dynamic simulation, and comparison, Energy 284 (2023) 128594.
[30] B. Widom, Equation of state in the neighborhood of the critical point, J. Chem. Phys. 43 (11) (1965) 3898–3905.
[31] Q. Wang, X. Ma, J. Xu, et al., The three-regime-model for pseudo-boiling in supercritical pressure, Int. J. Heat Mass Transf. 181 (2021) 121875.
[32] C. Yan, W. Wu, X. Zhang, et al., Investigation on supercritical CO_2 heat transfer crossing pseudo-critical temperature in vertical tubes assessed based on thermal resistance, Int. J. Therm. Sci. 210 (2025) 109632.
[33] Z. Yang, H. Wang, B. Guan, et al., Experimental and numerical investigation on the mechanisms of novel heat transfer deterioration of supercritical CO_2 in vertical tubes, Int. Commun. Heat Mass Transfer 153 (2024) 107384.
[34] D.T. Banuti, M. Raju, M. Ihme, Similarity law for Widom lines and coexistence lines, Phys. Rev. E 95 (5) (2017) 052120.
[35] X. He, J. Xu, X. Yu, et al., Distinguishing evaporation-like and boiling-like modes of pseudo-boiling in supercritical pressures, Int. J. Heat Mass Transf. 214 (2023).
[36] R. Rybár, M. Beer, D. Kudelas, et al., Copper metal foam as an essential construction element of innovative heat exchanger, Metalurgija 55 (3) (2016) 489–492.
[37] K. Li, Z. Zhu, B. Xiao, et al., State of the art overview material degradation in high-temperature supercritical CO2 environments, Prog. Mater. Sci. 136 (2023) 101107.

Nomenclature

Roman symbols

A: Contact area between the HSM and sCO_2 (m^2)
A_o: Outlet cross-sectional area(m^2)
c_v: Specific heat at constant volume of sCO_2 (kJ/(m^3·°C))
c_p: Specific heat at constant pressure of sCO_2 (kJ/(kg·°C))
$c_{p,hs}$: Specific heat at constant pressure of HSM (kJ/(kg·°C))
d_l: Ligament thickness of copper foam (mm)
G: The mass flow rate (kg/s)
h: The convective heat transfer coefficient (kW/m^2·°C)
h_c: Specific enthalpy of sCO_2 in the high-pressure tank (kJ/kg)
h_{t0}: Specific enthalpy of sCO_2 at inlet of the turbine(kJ/kg)
h_{t1}: Specific enthalpy of sCO_2 at outlet of the turbine(kJ/kg)
m: Mass (t)
m_c: The released mass of each time step (t)
Δm_{max}: The total released mass of CO_2 (t)
$\Delta m_{hs,\ max}$: The optimal released mass of the R-PST (t)
$\Delta m_{0,\ max}$: The optimal released mass for the conventional PST (t)
δm: The difference between $\Delta m_{hs,\ max}$ and $\Delta m_{0,\ max}$ at the same pressure (t)
P: Pressure (MPa)
ΔP: Pressure difference between initial and cut-off pressure of PST (MPa)
Q: The amount of heat transfer (kJ)
s: Specific entropy (kJ/(kg·°C))
T: Temperature (°C)
T_{pc}: The pseudo-critical temperature (°C)
T_+: The boundary temperature between two-phase-like and gas-like phase (°C)
T_-: The boundary temperature between liquid-like and two-phase-like phase (°C)
t: Time (s)
t_s: Time step (s)
U: Intrinsic energy (kJ)
u: Specific intrinsic energy (kJ/kg)
V: Volume (m^3)
W_T: The work output of turbine (kJ)

Greek symbols

β: Volume fraction
Δ: Finite difference
λ: Thermal conductivity (kW/(m·°C))
ρ: Density (kg/m^3)
ω: Energy storage density (kWh/m^3)
ξ: Volumetric heat capacity (kJ/m^3·°C)

Superscripts

$'$: The states before heat exchange
$''$: The states after heat exchange

Subscripts

c: Carbon dioxide
e: Cut-off
h: High-pressure tank
hs: Heat-storage material
H-PST: High-pressure storage tank
i: Initial
l: Low-pressure tank
L-PST: Low-pressure storage tank
max: Maximum
pc: Pseudo-critical
T: Turbine
u: Unreleased

Abbreviations

Bi: The Biot number
CAES: Compressed air energy storage
CCES: Compressed CO_2 energy storage
CGES: Compressed gas energy storage
CO_2: Carbon dioxide
CT: Cold tank
DN: Nominal diameter
ESD: Energy storage density
G_e: Generator
HE: Heat exchanger
HSM: Heat-storage material
H-PST: High-pressure storage tank
HT: Hot tank
LCES: Liquid CO_2 energy storage
L-PST: Low-pressure storage tank
M_e: Electric motor
PCMs: Phase change materials
PST: Pressure storage tanks
R-PST: Regenerative pressure storage tank
sCO_2: Supercritical carbon dioxide